RESEARCH ARTICLE

A Sea-Breeze Case Study in the La Plata River Region Using Local Observations, Satellite Images, and Model Simulations

Guillermo J. Berri[1] · Mariana Dezzutti[1]

Abstract

Two well-developed sea-breeze cases in the La Plata River region, selected from a 5-month summer period, are studied using local observations, satellite images, and hydrostatic boundary-layer model simulations. Both the northern and southern coast cases are characterized by offshore regional flow that help develop stronger sea breezes due to enhanced horizontal convergence by the opposing flow. The study shows that the sea-breeze propagation accompanies changes in the three-dimensional circulation within the boundary layer. The inland propagation speed of the cloud bands evident in satellite imagery is simulated relatively well by the model's progression of maximum vertical motion in both cases. Local coastline features affect the inland penetration of the sea-breeze fronts. The inland propagation speed of the surface sea-breeze front estimated with the model simulations is greater than the speed of the cloud bands aloft.

Keywords Case study · La Plata River · Modelling · Observations · Sea-breeze circulation

1 Introduction

The sea–land breeze is a mesoscale circulation usually observed in meteorological stations near coasts, because of the daily cycle of the surface temperature contrast between land and water. The difference of heat capacities between these surfaces gives rise to the formation of a low-level temperature gradient across the coast that results in the creation of a pressure gradient perpendicular to the coastline. The increase in magnitude of the pressure gradient creates a wind component from water to land, which prevails until late in the afternoon. At night, the local wind component reverses and the land breeze develops, although it is normally weaker than the sea breeze (Simpson 1994).

This mesoscale circulation is well defined during the day, so that the three-dimensional structure of the sea breeze can be schematically described as an alongshore vertical cell in which the air at low levels flows from water to land near the coast. The shallow wedge of cooler and humid maritime air moves inland tens of kilometres, creating a sea-breeze front

✉ Guillermo J. Berri
    gberri@fcaglp.unlp.edu.ar

[1] Facultad de Ciencias Astronómicas y Geofísicas – CONICET, Universidad Nacional de La Plata, Paseo del Bosque s/n, B1900FWA, La Plata, Argentina

at its leading edge and forcing updrafts, accompanied by local changes of wind, temperature, and humidity patterns (Miller et al. 2003). In order to keep the system in balance, a weaker return flow establishes aloft and an extended subsidence region over the sea closes the cell (Simpson 1994).

The sea-breeze circulation occurs in interaction with the regional environment and is conditioned by different factors, for example geography and topography (Miao et al. 2003; Bastin et al. 2005), time of year (Papanastasiou et al. 2010; Federico et al. 2010), direction and intensity of regional airflow (Srinivas et al. 2006), among others. These factors modify the structure of the sea breeze and sometimes cause irregularities that even prevent its development (Crosman and Horel 2010).

The La Plata River in South America (see Fig. 1 for location) is a large water surface 300 km long and of variable width between 50 and 200 km, that creates sufficient surface temperature contrast with the continent for setting up appropriate conditions for the development of a low-level circulation of sea–land breeze type. The regional scale environment of the La Plata River region is characterized by predominantly north-easterly low-level winds due to the influence of the semi-permanent subtropical South Atlantic anticyclone, as can be appreciated in Fig. 1, which shows the 1994–2008 mean sea level pressure taken from Reanalysis 2 (Kanamitsu et al. 2002). Berri and Bertossa (2018) analyzed the regional surface wind observations, and Fig. 2 (reproduced with permission from Fig. 2 of Berri and Bertossa 2018) presents the 1994–2008 mean wind direction roses observed in 13 weather stations of the La Plata River region during the period. Figure 2a, of the early morning at 0600 LT (local time = UTC − 3 h), shows predominant offshore winds, in particular over the northern coast. Instead, at mid-afternoon (1500 LT), Fig. 2b shows dominant onshore winds almost everywhere in the region. This notable direction change
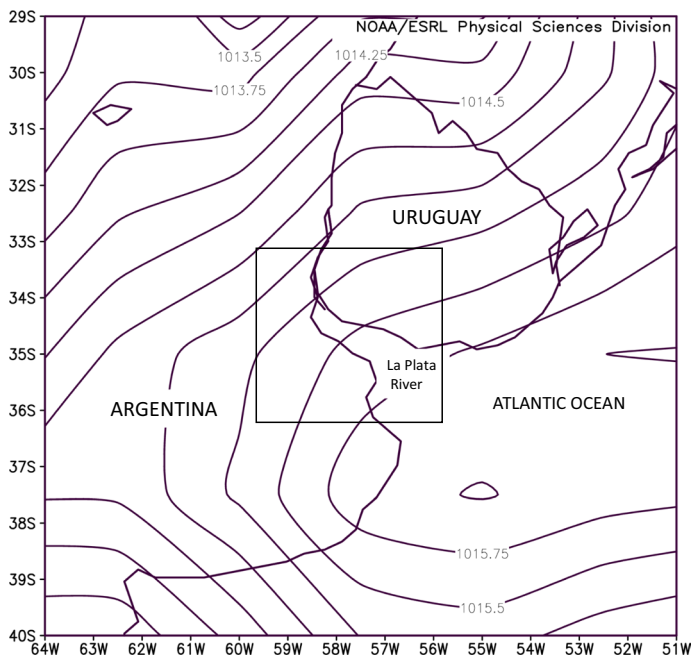
Fig. 1 1994–2008 mean sea level pressure (hPa) from NCEP/DOE 2 Reanalysis, data provided by the NOAA/OAR/ESRL PSD, Boulder, Colorado, USA
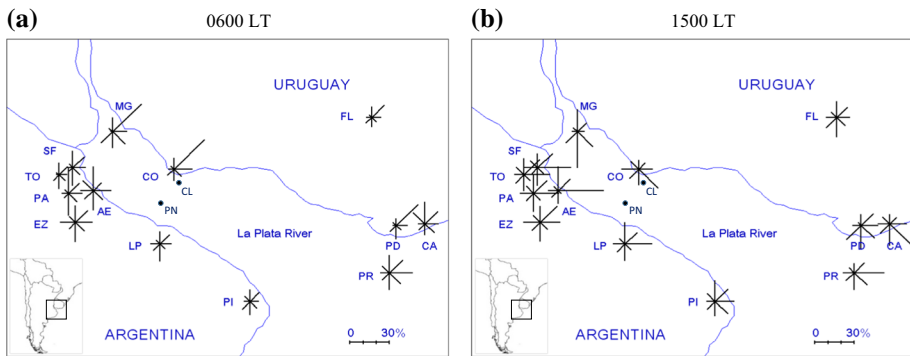
Fig. 2 Observed 1994–2008 mean wind direction frequencies at **a** 0600 LT and **b** 1500 LT. The bars indicate the wind direction with a relative frequency according to the percentage scale shown in the lower right corner of each panel. The surface weather stations are: Florida (FL), Carrasco (CA), Prado (PD), Colonia (CO), Martín García (MG), San Fernando (SF), Don Torcuato (TO), El Palomar (PA), Ezeiza (EZ), Aeroparque (AE), La Plata Aero (LP), Punta Indio (PI), and Pontón Recalada (PR). The river buoys, marked with dots, are Pilote Norden (PN) and Colonia (CL). The inner box in the lower left corner shows the location of the La Plata River in South America. (Reproduced with permission from Fig. 2 of Berri and Bertossa 2018)

of the predominant flow between the times of maximum and minimum temperatures is a clear indication of the significant role played by the sea–land breeze circulation in the local climatology of the La Plata River region.

The sea–land breeze is, among all the mesoscale phenomena, one of the most studied, both observationally and theoretically, due to the geographically fixed nature and repetitive characteristics of the event. There have been continuous advances in sea-breeze numerical modelling over the decades, from one-dimensional linear models to high-resolution non-hydrostatic three-dimensional models with full physics. Crosman and Horel (2010) present an extensive review of numerical studies. Berri et al. (2010) and Berri and Bertossa (2018) simulated the low-level circulation over the La Plata River region with the mesoscale boundary-layer model (hereafter, the model), and reproduced the observed climatological wind fields with reasonable accuracy. Sraibman and Berri (2009) ran daily low-level wind forecasts with the model over the La Plata River region during a summer period. The model, forced with operational Eta model regional forecasts, produced wind direction and wind speed forecasts at five weather stations of the region, with smaller error than Eta model itself. The study of Berri and Nuñez (1993) simulated low-level wind fields in the La Plata River region by running one experiment forcing the model with favourable boundary conditions for the sea-breeze set-up, i.e. anticyclonic conditions with sustained northeast light winds during the day. The simulated wind fields showed good agreement with the observed mean wind direction roses of six meteorological stations. The authors also found good agreement between the model vertical motion fields and the cumulus clouds seen in a mid-afternoon satellite image. These studies, aimed at simulating mean wind field patterns, concluded that the model is a useful tool for studying the low-level circulation in the region.

The objective of this research is to carry out a detailed analysis of the sea-breeze circulation over the La Plata River region with two case studies, using observations, satellite imagery, and model simulations. The selection of cases, from a 5-month summer period, is based on the analysis of cloud patterns of satellite images with the purpose of identifying

specific cases for which the dry hydrostatic model is likely to be relevant and perform well. The two selected cases, in both the northern and southern coasts, are characterized by off-shore regional winds that help develop stronger sea breezes due to enhanced horizontal convergence by the opposing winds.

The model is forced with initial and boundary conditions taken from the Eta operational forecast of the National Meteorological Service of Argentina. The forecasts are validated with hourly local observations and reanalysis. Time sequences of high-resolution GOES-13 images are used to compare the model upward motion fields with the time evolution of boundary layer clouds during the afternoon. Section 2 briefly describes the model, the data used, the methodology adopted for the selection of the two cases, and the definition of the sea-breeze front. Section 3 describes the forecasts validation with local weather observations and reanalysis, and Sect. 4 discusses the vertical structure of the sea-breeze circulation obtained with the model. Section 5 describes the results, and the summary and conclusions of the study are in Sect. 6.

2 Methodology

2.1 Data

The data include local meteorological observations and satellite imagery. The local observations consists of temperature, wind direction, and wind speed records of seven meteorological stations of the region (see location in Fig. 2), namely: Punta Indio (PIN), La Plata Aero (LPA), Ezeiza (EZE), Palomar (PAL), Aeroparque (AER), Colonia (COL), and Carrasco (CAR); two buoys of the La Plata River, Colonia (CL) and Pilote Norden (PN); and the 0900 and 2100 LT EZE radiosonde soundings. The satellite imagery consists of 30-min sequences of 1-km resolution GOES-13 images, and daily images of the MODIS sensor of the Terra satellite that orbits the region in the early afternoon.

2.2 Modelling and Experiment Design

The sea–land breeze cases are simulated with the model, which was specifically developed for simulating the low-level circulation over coastal regions. The model is based on a dry, hydrostatic boundary layer and includes the basic conservation equations of momentum, mass, and heat, with a first-order turbulence closure (see Berri and Nuñez (1993) and Berri et al. (2010) for details of the model). In brief, the model can be driven by prescribed upper and lower boundary conditions defined either from observations (Berri et al. 2010, 2012; Ratto et al. 2014; Berri and Bertossa 2018), or from other model forecasts (Sraibman and Berri 2009).

The domain of the model forecasts is the region depicted in Fig. 1, and consists of 89 in longitude and 58 in latitude grid points with horizontal resolution of 0.05º, 5-km in average. The vertical domain has 16 levels between the surface and the material top at 2000 m, distributed according to a log–linear spacing. The model initial and boundary conditions are taken from the operational Eta forecasts of the National Meteorological Service of Argentina. The lower boundary condition is defined from the Eta surface temperature and atmospheric pressure forecasts. The upper boundary condition, at the model top, is defined from the Eta 850-hPa wind and temperature forecasts, the closest Eta output level to what can be considered as the mean boundary layer height, since the other two available Eta

levels are 1000 hPa and 700 hPa. The Eta resolution of 0.66º of longitude and 0.33º of latitude is interpolated to the 0.05º model resolution with the Cressman (1959) method. The 3-h Eta outputs are interpolated to the 30-s the model timestep with cubic spline functions. At the lateral boundaries, variables are allowed to change in order to provide a zero gradient across the boundaries.

The sea-breeze component of the low-level model wind field is driven by the perturbation pressure (p'), associated to the potential temperature perturbation (θ'). Since the model is hydrostatic, the perturbed form of the vertical momentum equation (see Berri et al. 2010 for the details) is $\partial p'/\partial z = (g/\alpha_o)\,(\theta'/\theta_o)$, where $p' = p - p_o$, $\theta' = \theta - \theta_o$, g is the acceleration of gravity, and α is the specific volume. Subscript (o) refers to the horizontally averaged value over the entire domain, and superscript (') refers to the local departure from the average. Regions over land and near the coast warm up during the day ($\theta' > 0$), while neighbouring regions over water remain practically unchanged ($\theta' = 0$). At every timestep, the equation is integrated downwards from the unperturbed model top (2000 m) to the surface (where the land–water thermal contrast is the main driving mechanism), so that $\delta\Delta p' = -(g/\alpha_o)\,(\theta'/\theta_o)\,|\delta z|$. Thus, over the warmer region $\delta p' < 0$, i.e., $p' < 0$ at the surface since $p' = 0$ at the unperturbed top, resulting in a surface pressure drop over land that drives the sea-breeze wind component blowing from water to land.

It is widely acknowledged that hydrostatic models have limitations in adequately reproducing sea-breeze dynamics, particularly the vertical motion that is a substantial component. Pielke (2002) analyzes the results of nonlinear see-breeze models with and without the hydrostatic assumption, indicating that the relationship between horizontal and vertical scales is decisive for the validity of the hydrostatic assumption. In particular, Orlanski (1981) is more restrictive and indicates that the ratio between the vertical motion scale H and the horizontal grid spacing Δs must comply with $H/\Delta s < < 1$, before the hydrostatic assumption can be applied with precision. The model has a vertical domain size of 2 km and a horizontal grid resolution of 5 km, so that such condition is fulfilled. Martin and Pielke (1983) analyze the adequacy of the hydrostatic assumption in sea-breeze modelling over flat terrain, as the case of the La Plata River region, using a nonlinear analytic model to evaluate the relative error in the vertical velocity between non-hydrostatic and hydrostatic models. The authors highlight the importance of a stable thermodynamic stratification since an $H/\Delta s$ ratio close to unity can still provide nearly identical solutions, regardless of whether or not the hydrostatic assumption is used. In other words, the more stable the atmosphere, the lower the error of the vertical velocity calculated with a hydrostatic model compared to a non-hydrostatic one. In the present simulations, the vertical gradient of potential temperature calculated with the 0900 LT Ezeiza radiosonde sounding, averaged of the 2-km model domain is $+0.22$ K/100 m for the 7 November 2015 case, and $+0.54$ K/100 m for the 11 January 2016 case. According to Martin and Pielke (1983), the relative error between hydrostatic and non-hydrostatic vertical velocities would be less than 3% for a 5-km horizontal grid resolution.

2.3 Selection of Sea-Breeze Cases

In order to identify the sea-breeze cases, the 5-month summer period from November 2015 to March 2016 is used, because it is the most recent one in our database. The selection of the sea-breeze cases is done in two steps. In first place we use the MODIS image of the early afternoon to identify days with cumulus humilis cloud bands typically associated with sea-breeze circulations (Simpson 1994). These clouds are characterized by a small

vertical extent that never produce precipitation, and its spatial pattern and time evolution in the region are discussed in the following sections. The first condition of the selection procedure targets the specific cases for which the dry model is likely to be relevant and perform well.

In the second step, the analysis of local meteorological observations allowed to filter out the appropriate days from the preselected group of days based on the cloud pattern analysis of MODIS images. The literature presents different methods for identifying days with appropriate conditions for the development of the sea-breeze circulation. For example, Lyons (1972) uses the presence of an upper return flow; Furberg et al. (2002) point out that the diurnal wind direction change is the most important criterion for the selection; and Prtenjak and Grisogono (2007) select cases by screening surface observations of temperature, wind direction, wind speed, atmospheric pressure, sea surface temperature, and cloudiness, together. The present study adopts the criteria proposed by Borne et al. (1998) that uses wind and temperature observations and their time evolution to determine appropriate conditions for sea-breeze development. We believe that these criteria, which are summarized as follows, are sufficiently detailed and appropriate for the study:

1. 700-hPa geostrophic wind direction changes $< 90°$ during a 24-h period (from 1300 LT of previous day until 1300 LT of present day),
2. 700-hPa geostrophic wind speed changes < 6 m s^{-1} during a 12-h period (from 0100 LT until 1300 LT of the present day),
3. 700-hPa geostrophic wind speed < 11 m s^{-1} until 1300 LT,
4. maximum surface temperature of the present day at a land station (T_x), and surface temperature at a station over the water (T_w), must fulfil the relationship $T_x - T_w > 3$ °C, during the previous 24-h period,
5. surface wind direction changes at a land station $> 30°$ from 1 h after sunrise until 5 h before sunset,
6. the relationship between the sharp change of surface wind direction (WD_s) and the mean change of surface wind direction (WD_m) during the 5-h period following the sharp change, at a land station, must fulfil the relationship $WD_s/WD_m > 6$.

The first three conditions filter out days in which changes of the synoptic scale conditions may prevent or modify the sea-breeze development. The fourth condition guarantees sufficient surface temperature contrast for the sea-breeze set up, and the last two conditions guarantee that local wind direction changes during the day are consistent with the observations of sea-breeze episodes.

The sequence of satellite images complement the observations of the limited number of surface stations available in the region and allow determination of the presence of the spatial cloud pattern typically associated with the sea breeze, facilitating the study in a regional context. The flow convergence of the sea-breeze front causes air rise and, in the presence of available moisture, cloud formation (Miller et al. 2003). Cloud lines parallel to the coast on a basically cloudless day can be a clear indication of the sea-breeze presence, whose spatial extension is possible to infer from the cloud pattern (Nicholls et al. 1991; Wakimoto and Atkins 1994; Planchon et al. 2006, among others). The interpretation of these cloud patterns also allows inferring the inland reach of the sea breeze.

The predominant regional wind plays a major role in determining the position relative to the coastline of the sea-breeze circulation (Estoque 1962; Arritt 1993; Srinivas et al. 2006, among others). The regional wind is important for determining if the sea breeze will be

detectable on land, and to what extent it could influence its behaviour (Finkele et al. 1995). For example, an offshore regional wind (directed from land to sea) increases horizontal flow convergence by opposing the sea-breeze component and makes it stronger, although a very strong offshore wind may prevent the sea breeze from reaching the coast. On the other hand, an onshore wind (directed from sea to land) allows the sea breeze to move farther inland. In particular, Finkele (1998) discusses inland and offshore propagation speeds indicating that the inland sea-breeze extent is greater in light offshore geostrophic winds than in moderate ones, although with offshore geostrophic winds stronger than 7.5 m s^{-1}, the sea breeze is completely offshore.

The analysis of MODIS images identified 31 days during the period of November 2015 to March 2016 with early afternoon cloud patterns that could be associated with sea-breeze events over the La Plata River region. Then, the analysis of 30-min sequences of GOES-13 images, in search of a clearly identifiable evolution of cloud bands during the day, reduced the initial set to seven potential cases for the study. Finally, the application of Borne et al. (1998) criteria left only two cases that we consider appropriate because they not only fulfilled all the imposed conditions but also had the most complete records of meteorological observations.

The selected days are 7 November 2015 with a north-north-east regional wind (onshore the southern coast, offshore the northern coast), and 11 January 2016 with a south-west regional wind (offshore the southern coast, onshore the northern coast).

3 Model Validation

The model forecasts are validated with the wind and temperature observations of seven land stations, two buoys in the La Plata River and twice daily radiosonde soundings of the Ezeiza airport (EZE), at 0900 LT and 2100 LT. At the regional scale, the 850-hPa Eta forecasts, the driving upper boundary conditions of the model, are validated with Reanalysis 2 (Kanamitsu et al. 2002).

Figure 3 compares the 850-hPa Eta geopotential forecast with the 6-h reanalysis of 0900, 1500 and 2100 LT of 7 November 2015 (Fig. 3a) and 11 January 2016 (Fig. 3b). The reanalysis (Fig. 3a) shows a high-pressure system over the La Plata River at 0900 LT that moves eastward in the afternoon, and northerly winds over the region during the day. In the 11 January 2016 case (Fig. 3b), the reanalysis shows a high-pressure system to the north-west of La Plata River that moves eastward during the day, and sustained westerly flow in the area. In both cases, the Eta forecasts show very good agreement with the reanalysis, so that the upper boundary conditions of the model are qualitatively correct at the regional scale. The Eta surface temperature forecasts, the driving lower boundary condition of the model, also show good agreement with the reanalysis, but these figures are not shown, because the coarse resolution of reanalysis plots only reveal regional scale aspects.

Table 1 show small differences between the 850-hPa Eta forecast and EZE radiosonde soundings, less than 2 m s^{-1} in wind direction and about 1 °C or less in temperature. In addition, the observed increase in wind speed and temperature between 0900 and 2100 LT is correctly reproduced by the Eta forecast.

0900 LT	1500 LT	2100 LT
(a) 7 November 2015		
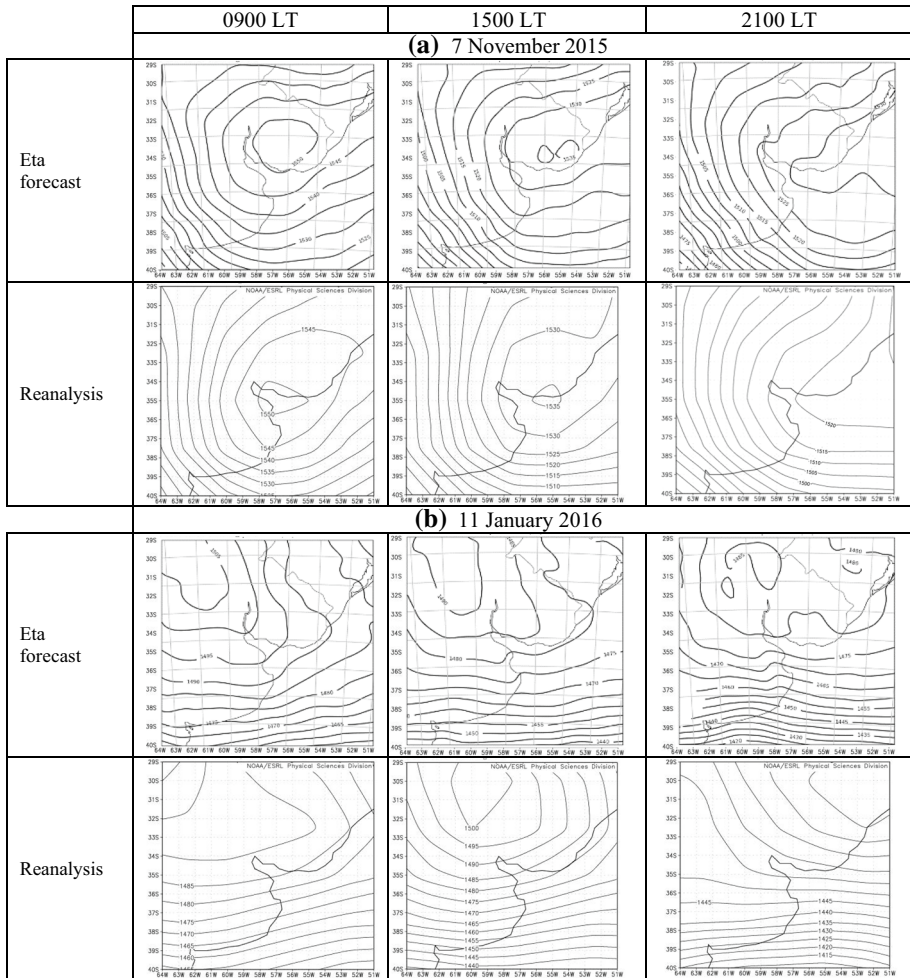
Fig. 3 **a** Eta 850-hPa geopotential forecast for 0900 LT (left box), 1500 LT (centre box), and 2100 LT (right box) of the 7 November 2015 case, and corresponding reanalysis from NCEP/DOE 2 Reanalysis, data provided by the NOAA/OAR/ESRL PSD, Boulder, Colorado, USA; **b** same as **a** but for the 11 January 2016 case

3.1 Validation with Surface Observations

The model surface wind and temperature forecasts are validated with the observations of seven land stations, namely Punta Indio (PIN), La Plata Aero (LPA), Ezeiza (EZE), Palomar (PAL), Aeroparque (AER), Colonia (COL), and Carrasco (CAR). The data of two buoys in the La Plata River, Pilote Norden (PN), and Colonia (CL), is also used, which only have wind observations (see locations in Fig. 2). There are hourly observations from 0900 to 2100 LT, except in the case of CAR and COL that only have 3-h observations available.

Table 1 Comparison of 850-hPa level wind direction (*WD*), wind speed (*WS*), and temperature (*TEMP*) of the 0900 LT and 2100 LT EZE radiosonde sounding with Eta forecasts, for the 7 November 2015 and 11 January 2016 cases

	0900 LT			2100 LT		
	WD (°)	*WS* (m s^{-1})	*TEMP* (K)	*WD* (°)	*WS* (m s^{-1})	*TEMP* (K)
7 November 2015						
EZE sounding	10	2.5	296.4	350	7.0	298.1
Eta forecast	340	2.0	296.8	350	5.0	297.7
11 January 2016						
EZE sounding	240	3.0	302.9	285	6.5	305.6
Eta forecast	270	2.5	302.5	280	4.5	306.0
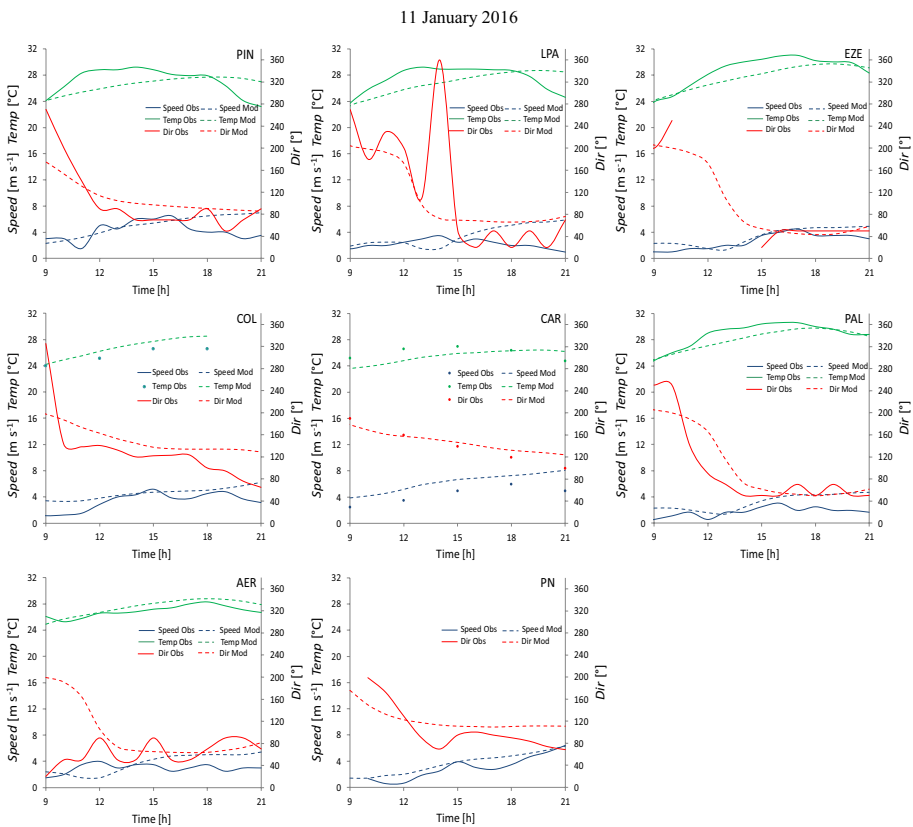
Fig. 4 Comparison of the model forecast and observations of wind direction (red), wind speed (blue), and temperature (green) of meteorological stations of Punta Indio (PIN), La Plata Aero (LPA), Ezeiza (EZE), Colonia (COL), Carrasco (CAR), Palomar (PAL) and Aeroparque (AER), and La Plata River buoy Pilote Norden (PN), for the 11 January 2016 case. Full lines correspond to observations, dashed lines to the model, and dots to 3-h observations. Wind direction and wind speed of the COL panel correspond to La Plata River buoy Colonia (CL), see text for the details
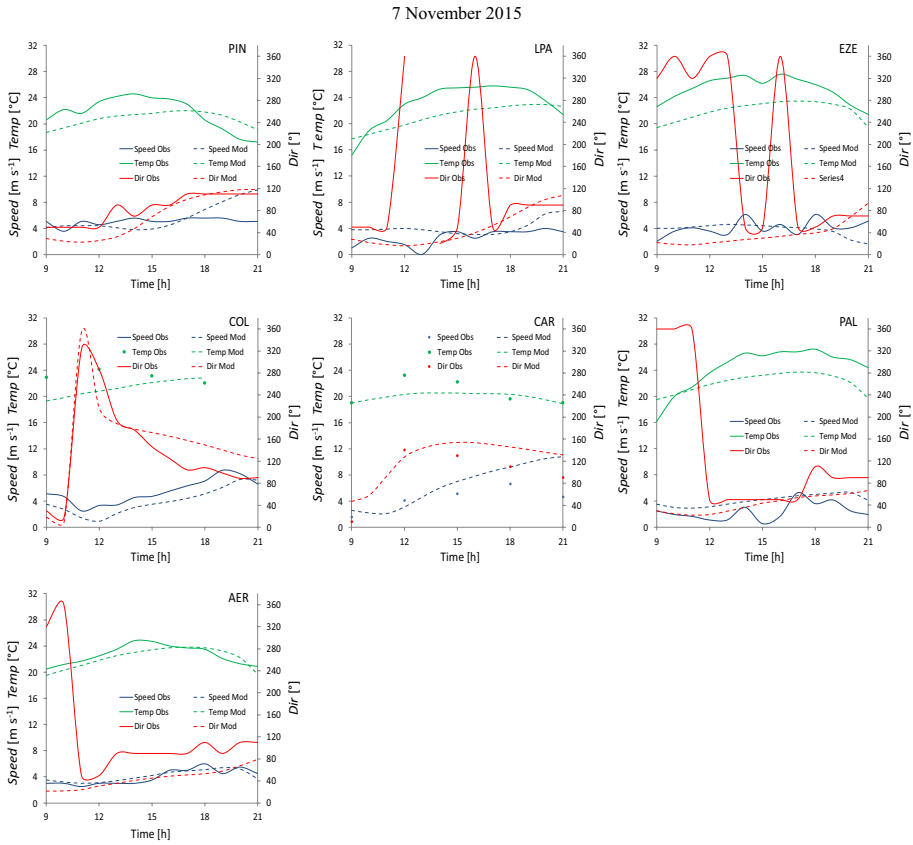
7 November 2015

Fig. 5 Same as Fig. 4 for, the 7 November 2015 case

Figures 4 and 5 compare the model wind and temperature forecasts with hourly observations of 11 January 2016 and 7 November 2015, respectively. The accuracy measures to evaluate the model performance are among the most commonly used (Wilks 2011). One is the mean absolute error (*MAE*) of wind direction, wind speed, and temperature, defined as the arithmetic average of the absolute differences between pairs of forecast (*F*) and observed (*O*) values:

$$MAE = \frac{1}{N} \sum_{j=1}^{N} |F_j - O_j|, \tag{1}$$

where *N* is the number of observations available. The other measure is the r.m.s. error (*RMSE*) of wind and temperature:

$$RMSE_{\text{temp}} = \sqrt{\frac{1}{N} \left(\sum_{j=1}^{N} \left(T_f - T_o \right)_j^2 \right)} \tag{2}$$

$$RMSE_{\text{wind}} = \sqrt{\frac{1}{N}\left(\sum_{j=1}^{N}\left(U_f - U_o\right)_j^2 + \sum_{j=1}^{N}\left(V_f - V_o\right)_j^2\right)}, \tag{3}$$

where U, V are the wind components, T is temperature, N the number of observations available and subscripts f and o refer to forecast and observation, respectively. The $RMSE$ has the advantage of being more sensitive to larger errors by squaring them, while the $RMSE_{\text{wind}}$ combines both wind direction and wind speed, as indicated by (3).

Tables 2 and 3 summarize the model performance showing the daily averaged errors of wind direction, wind speed, and temperature for the 11 January 2016 and 7 November 2015 cases, respectively, complemented with the daily maximum (*MAX*) and the daily minimum (*MIN*) values of the absolute difference between forecast and observation.

3.1.1 The 11 January 2016 Case

Figure 4 compares the model forecasts with observations of wind direction (red), wind speed (blue), and temperature (green) for the 11 January 2016 case, in one panel for each station, with the following exception. Since the CL buoy (hourly observations) is very close to COL (3-h observations), for simplicity the three variables are shown together in the COL panel, such that temperature corresponds to COL and wind to CL. It should be noted that EZE has no wind direction data between 1100 and 1400 LT, and the 3-h observations of CAR and COL are plotted with dots.

Table 2 Daily averaged model errors of wind direction, wind speed, and temperature

11 January 2016	PIN	LPA	EZE	COL	CAR	PN	PAL	AER
Temperature (°C)								
MAE_{temp}	1.5	1.1	1.0	1.1	1.0	–	0.8	0.8
MAX_{temp}	3.3	2.9	1.8	1.9	1.3	–	1.9	1.3
MIN_{temp}	0.2	0.0	0.0	0.2	0.0	–	0.0	0.1
Temperature (°C)								
$RMSE_{\text{temp}}$	1.8	1.4	1.6	1.2	1.0	–	1.1	0.7
Wind direction (°)								
MAE_{wd}	27	32	13	24	11	25	27	46
MAX_{wd}	95	98	50	53	24	48	76	179
MIN_{wd}	1	0	0	11	3	4	0	6
Wind speed (m s^{-1})								
MAE_{ws}	1.6	2.0	0.8	3.6	2.6	0.6	1.5	1.3
MAX_{ws}	3.8	4.7	1.9	4.8	6.6	1.5	3.0	2.5
MIN_{ws}	0.2	0.5	0.0	1.5	1.3	0.0	0.3	0.0
Wind $RMSE$ (m s^{-1})								
$RMSE_{\text{wind}}$	3.4	3.3	1.4	3.9	3.5	2.1	1.9	2.8

The meteorological stations are Punta Indio (PIN), La Plata Aero (LPA), Ezeiza (EZE), Colonia (COL), Carrasco (CAR), Palomar (PAL) and Aeroparque (AER), and La Plata River buoy Pilote Norden (PN), for the 11 January 2016 case. Wind direction and wind speed of COL correspond to La Plata River buoy Colonia (CL), see text for the details

Table 3 Same as Table 2, for the 7 November 2015 case

7 November 2015	PIN	LPA	EZE	COL	CAR	PAL	AER
Temperature (°C)							
MAE_{temp}	2.2	2.4	3.3	2.1	1.1	2.8	0.9
MAX_{temp}	3.2	4.5	4.8	3.6	2.9	4.7	1.8
MIN_{temp}	1.0	0.6	0.6	0.8	0.0	0.2	0.1
Temperature (°C)							
$RMSE_{temp}$	2.3	2.8	3.5	2.5	1.7	3.1	1.0
Wind direction (°)							
MAE_{wd}	18	22	25	31	30	16	38
MAX_{wd}	58	50	62	70	41	49	57
MIN_{wd}	1	4	1	2	13	1	19
Wind speed (m s^{-1})							
MAE_{ws}	1.5	1.4	1.3	1.6	2.5	1.8	0.5
MAX_{ws}	4.8	3.9	3.5	2.6	6.2	3.6	0.9
MIN_{ws}	0.0	0.3	0.1	0.6	0.9	0.5	0.1
Wind speed (m s^{-1})							
$RMSE_{wind}$	2.8	2.3	2.7	3.6	4.6	2.2	2.9

In general, the model reproduces the observed wind changes relatively well, even though at some times of the day and in some places, the errors are large. The 11 January 2016 case shows substantial wind direction rotation from the south-west in the morning, through the south, towards the east and the north-east by noon, everywhere, remaining so during the rest of the afternoon. This substantial wind direction change of more than two quadrants is well represented by the model, as can be seen in Fig. 4. The plot of observed wind direction in the LPA panel suggests around noon, a 300° wind shift in one hour, but is actually of 120°. There is a counter-clockwise (CCW) wind rotation in the previous hours from the south-west, across the south, to the east-south-east, and after that, despite a 1-h excursion to the north, the wind direction remains in the east quadrant during the rest of the afternoon. This potential misinterpretation is the consequence of displaying a cyclic variable as wind direction, in a linear plot that ranges between 0° (calm wind) and 360° (north wind).

The biggest discrepancy in wind direction is at AER during the morning hours when the observations show north-east and east-north-east wind, while all other stations show south-west and south-south-west wind. AER is the closest land station to the river, only a few hundred metres from the coast, and shows the wind direction shift due to the sea breeze earlier than the other places, since the previous observations at 0700 and 0800 LT (not shown) report south-west and west wind, respectively. Except for AER, the other stations show a CCW wind shift from south-west and south-south-west in the morning, throughout the south, towards the east and north-east in the afternoon, which is well reproduced by the model.

The observed wind speed changes during the day are less marked. PN shows a wind speed increase from about 2 to 6 m s^{-1}, while EZE, PAL, and AER show almost no change, all of which is well reproduced by the model. Instead, PIN, LPA, and CAR show a minor decrease of wind speeds in the late afternoon, not seen in the model forecast.

The temperature forecasts generally follow well the observed changes, although the daily amplitude is slightly smaller and the maximum temperature occurs rather later, with better results at EZE, PAL, and AER, and large errors towards late evening at PIN and

LPA. The study of Berri and Bertossa (2018) finds larger model errors towards dusk, attributed to the model weakness to adequately reproduce the transition to stable conditions, which would explain the large errors in the late afternoon. The amplitude and phase of the model daily temperature cycle are largely controlled by the boundary conditions that are defined from the 3-hourly Eta forecasts. The smooth aspect of the model forecast, without the small hourly oscillations as observed in most stations, is probably a consequence of its hydrostatic formulation that, as discussed in Sect. 2.2, prevents internal gravity waves from fully developing.

In the case of wind direction (Table 2), MAE_{wd} is less than 30° everywhere, except at AER due to large errors in the morning, as discussed above, and MAX_{wd} is about one quadrant. The MIN_{wd} is very small everywhere, only a few degrees, as well as the MIN_{ws} that in most places is less than 1.0 m s^{-1}, except at COL and CAR. In the case of wind speed, the MAE_{ws} exceeds 2 m s^{-1} only at COL and CAR, which also have the largest MAX_{ws} and MIN_{ws}. It should be noted that CAR has only five observations and COL only four, while the other stations have 13 observations, and that the smaller samples make those results less representative. The $RMSE_{wind}$ varies between 1.4 m s^{-1} in EZE and 3.9 m s^{-1} in COL, in four stations is below 3.0 m s^{-1}, and the $RMSE_{temp}$ varies between 0.7 °C and 1.8 °C and in three places is below 1.2 °C.

3.1.2 The 7 November 2015 Case

Figure 5 compares the model forecasts and observations for 7 November 2015, in one panel for each station, but in this case there are no PN observations available. As in the previous case, the COL panel includes the CL wind observations.

The same considerations made in the previous case, applies to the present one, regarding the correct interpretation of the large wind direction jumps observed in LPA (missing 1100 LT observation), EZE, PAL and AER, since Table 3 shows MAX_{wd} values between 41° and 70° there. The changes of wind direction observed during the day are well reproduced by the model, more evidently in PIN, COL and CAR. The stations of the southern coast show a CW wind shift throughout the day, less marked in EZE, while the two stations on the northern coast show the opposite CCW wind shift. As in the previous case, the small-amplitude oscillations displayed by the wind observations in most places are absent in the model forecasts.

Table 3 shows, in contrast to the other case, slightly smaller MAE_{wd} and MAX_{wd}, and relatively larger MAE_{ws} and MAX_{ws} in most places, while the $RMSE_{wind}$ is greater in four out of seven places. CAR presents the maximum $RMSE_{wind}$ of 4.6 m s^{-1} while in other places it varies between 2.2 and 3.6 m s^{-1}. The $RMSE_{temp}$ varies between 1.0 and 3.5 °C, and is larger everywhere in comparison to the other case. With the exception of AER, which shows the best agreement between forecasts and observations (see Fig. 5), the daily temperature change in the southern coast is over 6 °C (11 °C in PAL), which the model underestimates by about 2 °C. In the northern coast, the observed daily temperature change is small, which the model overestimates in COL and underestimates in CAR by about 2 °C. In addition, the model temperatures increase smoothly with time, in contrast to the small oscillations seen in the observations, and always reach their maximum later, as in the previous case.

The averaged $RMSE_{wind}$ of all the stations is 3.0 m s^{-1}, slightly larger than the 2.8 m s^{-1} of the other case, with the largest errors in CAR and COL in both cases. In the case of

temperature, the average $RMSE_{\text{temp}}$ of 2.4 °C almost doubles the 1.3 °C of the other case. We can only attribute the large difference between the two cases to possible errors of the Eta surface temperature forecast, difficult to appreciate due to the coarse resolution of reanalysis.

3.2 Comparison with Errors of Other Studies

In order to complement the evaluation of the quality and reliability of the model forecast, we compare it with the results reported by other studies of similar cases. Case studies of the lake breeze over Lake Michigan using the MM5 model find $RMSE_{\text{wind}}$ values between 1.0 and 3.6 m s^{-1} (Harris and Kotamarthi 2005), and between 1.7 and 2.5 m s^{-1} (Shafran et al. 2000); while a similar study using the RAMS model finds $RMSE_{\text{wind}}$ values between 1.3 and 2.2 m s^{-1} (Lyons et al. 1995). Harris and Kotamarthi (2005) report wind direction errors between 20° and 62° in two case studies of the Lake Michigan sea breeze. Other studies of the sea breeze using MM5 find a $RMSE_{\text{wind}}$ of 1.6 m s^{-1} in Thailand (Phan and Manomaiphiboon 2012), and 1.3 m s^{-1} in the Pearl River Delta of China (Xun-lai et al. 2009). A study of the influence of sea-breeze circulation in the Houston area using the ARW-WRF model finds a $RMSE_{\text{wind}}$ of 1.6 m s^{-1} (Chen et al. 2011). Those studies also calculate temperature errors obtaining $RMSE_{\text{temp}}$ values between 1.1 and 1.7 °C, although Harris and Kotamarthi (2005) report errors of up to 4.6 °C. In particular, Shafran et al. (2000) and Lyons et al. (1995) calculate only MAE_{temp} and report values between 1.5 and 2.3 °C. Sraibman and Berri (2009) run experiments in the La Plata River region with the model forced by Eta operational forecasts during a 6-month summer period and obtain a $RMSE_{\text{wind}}$ of 3.5 m s^{-1}, which is the average value obtained in four meteorological stations that participate in the present study.

The magnitude of wind and temperature errors of the present study do not differ much from what the other studies report, although in some cases ours are slightly larger. Since most of the studies used high-resolution non-hydrostatic models, we can affirm that the model forecasts are sufficiently reliable for the purpose of the present study.

4 Vertical Structure of Sea-Breeze Circulation

The simplified pattern of a sea-breeze front embedded in a well-organized alongshore vertical cell, steadily moving with sustained density currents under offshore ambient winds, certainly facilitates the understanding but omits relevant fine scale details of the phenomenon. Simpson (1994) describes a sea-breeze front characterized by trains of Kelvin–Helmholtz billows that develop at the shear zone between low-level onshore winds and ambient flows aloft and propagate seaward. This mechanism induces disturbances that define a more complex three-dimensional structure of the sea breeze composed of fine-scale lobes and clefts under alongshore ambient winds, characterized by short-term oscillations of ascending and sinking motions primarily driven by the repeated arrivals of gravity current disturbances.

A recent study of Chen et al. (2019) reveals the complexity of the sea-breeze front with high-resolution coupled mesoscale-to-large-eddy simulations and lidar observations in Japan. The authors describe a series of lobes, spaced approximately 500 m apart and aligned along the raised sea-breeze head, with local strong updrafts in the frontal lobes of

marine cold air and in the prefrontal warm air, and downdrafts formation behind the lifted marine cold air.

Certainly, these fine-scale details are beyond the capacity of a hydrostatic model such as the boundary-layer model. However, the geography of the region with flat terrain and relatively straight coastlines, gives the model a greater degree of reliability to represent the regional scale structure of the sea breeze and its changes with time, particularly in days that are widely recognized as appropriate for the occurrence of the phenomenon, as the two cases analyzed.

Figure 6 shows a model vertical cross-section at 34.95° S, with vectors defined by the horizontal wind component u and the vertical wind component w, for 11 January 2016 at 1845 LT (late afternoon of a summer day). In order to better appreciate the vertical structure of the sea-breeze circulation, the vector scale of the horizontal motion is in m s^{-1} and the vertical motion in cm s^{-1}. The horizontal separation between wind vectors plotted every other grid point is 9 km so that the graph expands 110 km over land and 80 km over the river. Inland, the westerly winds throughout the boundary layer are weak (see Fig. 3b), but in the lower levels towards the river the sea breeze gives rise to a region easterly wind component. Its leading edge, about 60 km inland (halfway inland in Fig. 6), creates a horizontal convergence zone forcing the upward motion that reaches its maximum at about 1 km. A return flow towards the east establishes aloft and the vertical circulation cell closes with an extended subsidence region over the river throughout the whole boundary layer.
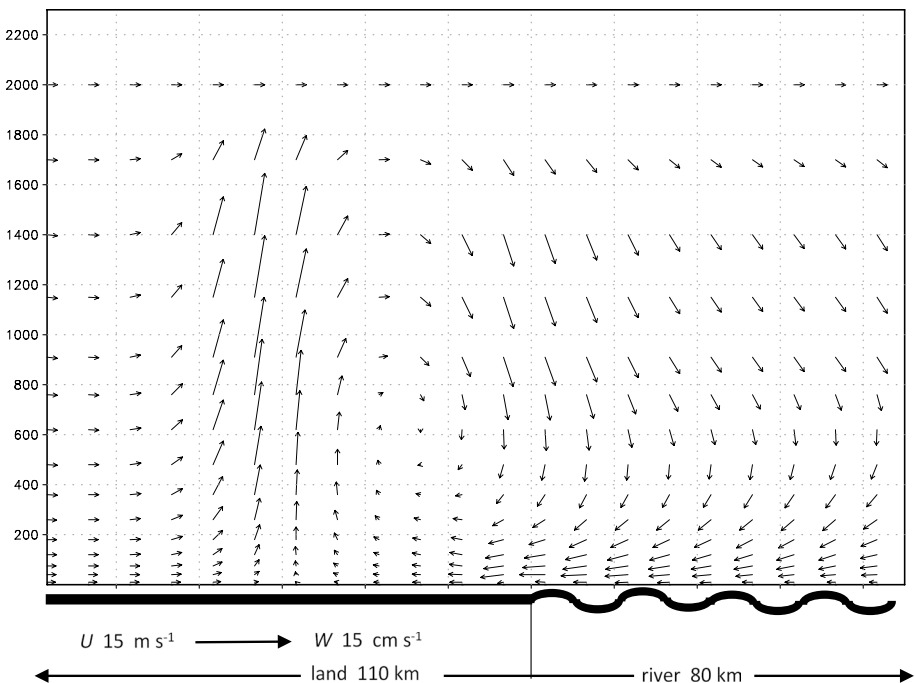

Fig. 6 The model vertical cross section of horizontal wind component u (vector scale in m s^{-1}) and vertical wind component w (vector scale in cm s^{-1}), at 34.95°S for 11 January 2016 1845 LT. The horizontal separation between wind vectors plotted every other grid point is 9 km

The vertical extent of the circulation cell is variable and depends on the local topographic characteristics and the weather conditions. For example, in the case of large lakes and open coasts it can be 200–500 m (Lyons 1972; Keen and Lyons 1978), in moderately warm climates it extends over 1000 m, while on the coasts of tropical regions it reaches heights of 1300–1400 m (Frizolla and Fisher 1963; Barbato 1978; Banta et al. 1993). Kunhikrishnan et al. (2006) find in the Arabic coasts a vertical extent of sea-breeze circulation of around 1000 m over sea as well as on land; although some measurements show that it can be of up to 2000 m (Defant 1951; Atkinson 1981; Comer and McKendry 1993). The vertical extent of the sea breeze is variable during the day, for example Zhong and Takle (1992) find in the morning heights between 500 and 600 m, growing up to 1 km by noon and decreasing to 800 m in the late afternoon.

5 Results

The inland progression of the surface sea-breeze front (hereinafter SBrF) and the associated displacement of boundary layer cloud bands are calculated along five transects perpendicular to the coast across the EZE, LPA, PIN, COL, and CAR meteorological stations (see Fig. 7a). The position of SBrF is determined with hourly the model surface wind fields. According to condition *v*) of Borne et al. (1998) criteria in Sect. 2.3, the grid point showing a wind direction change of at least 30° from the previous hour defines the position of the SBrF (dotted line in Fig. 7b), provided that in the downstream grid point the wind direction has not yet changed.

The 30-min sequence of GOES-13 images allows for identification of the position of the cloud front aloft (hereinafter CloF), as the point along transects such that towards the river the sky is cloudless (dashed line in Fig. 7b). Since the model is a dry model and therefore unable to simulate clouds, alternatively we define the maximum upward motion front (hereinafter WmxF), as the line across the region of maximum model upward motion at 1000 m (see Fig. 8), considering that its inland progression with time has to be associated
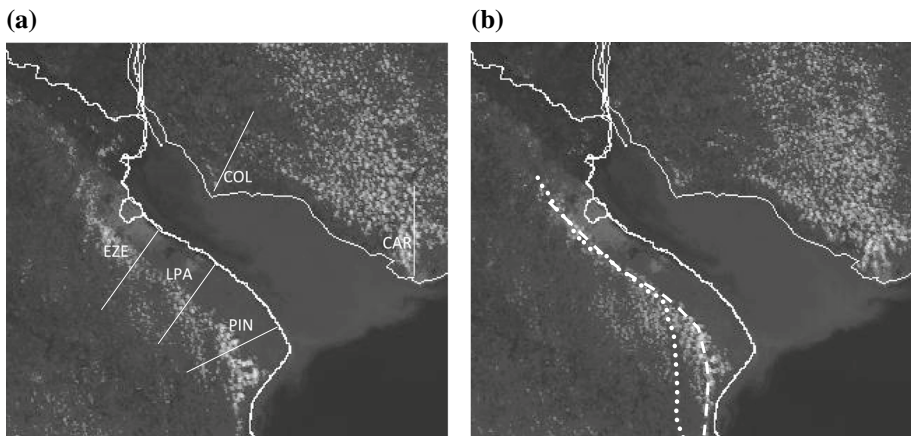
Fig. 7 a Perpendicular transects to the coast across the meteorological stations EZE, LPA, PIN, COL and CAR; **b** position of the surface sea-breeze front (dotted line) and the cloud band edge (dashed line), as seen on the GOES-13 image of 11 January 2016 1400 LT
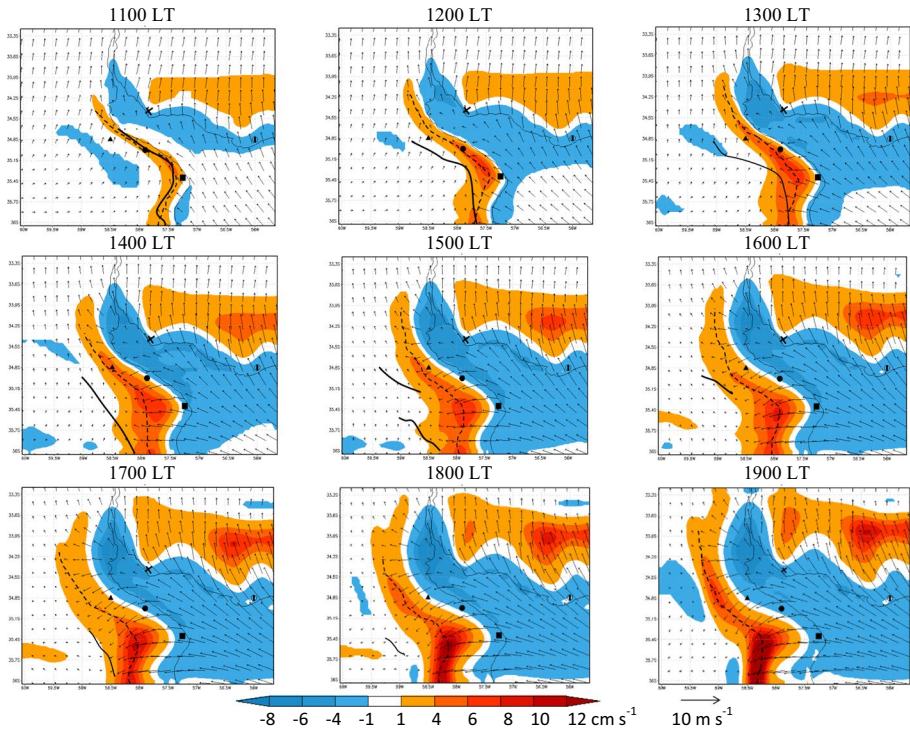
Fig. 8 Model wind field at 10 m and vertical velocity contours (cm s^{-1}) at 1000 m of the 11 January 2016 case. The full line represents the position of the surface sea-breeze front (SBrF) and the dashed line the maximum upward motion front (WmxF) in the southern coast. The meteorological stations are PIN (filled square), LPA (filled circle), EZE (filled triangle), COL (**x**), CAR (filled oval)

with the time evolution of the boundary layer cloud pattern. The distance along transects between the SBrF, CloF and WmxF positions and the coast is calculated, and distance versus time graphs are constructed that allow calculating the speed at which the fronts move forward.

Figure 8 shows hourly model outputs of surface wind fields (10 m) and vertical velocity contours (1000 m) of 11 January 2016 in the southern coast, in which the full line represents the SBrF position and the dashed line the WmxF position. Initially, both fronts are well defined and their layout follows the coast geometry, although later in the afternoon the SBrF is less defined. At 1100 LT the region of surface winds convergence (i.e., the SBrF) extends a short distance inland the southern coast. This convergence region is determined by the confluence of east and south-east winds over the river and south-west winds inland. The horizontal divergence dominates over the river, and this whole region is characterized by subsiding motion. During the following hours, both fronts move inland, although the SBrF does it faster, and the subsidence region strengthens over the river.

During the rest of the afternoon both fronts continue propagating inland, but around 1800 LT the SBrF loses spatial continuity, as over the south-west part of the domain the regional southwesterly wind shifts to the north-east, in the same direction of the SBrF propagation, weakening the horizontal convergence region. The region of maximum upward
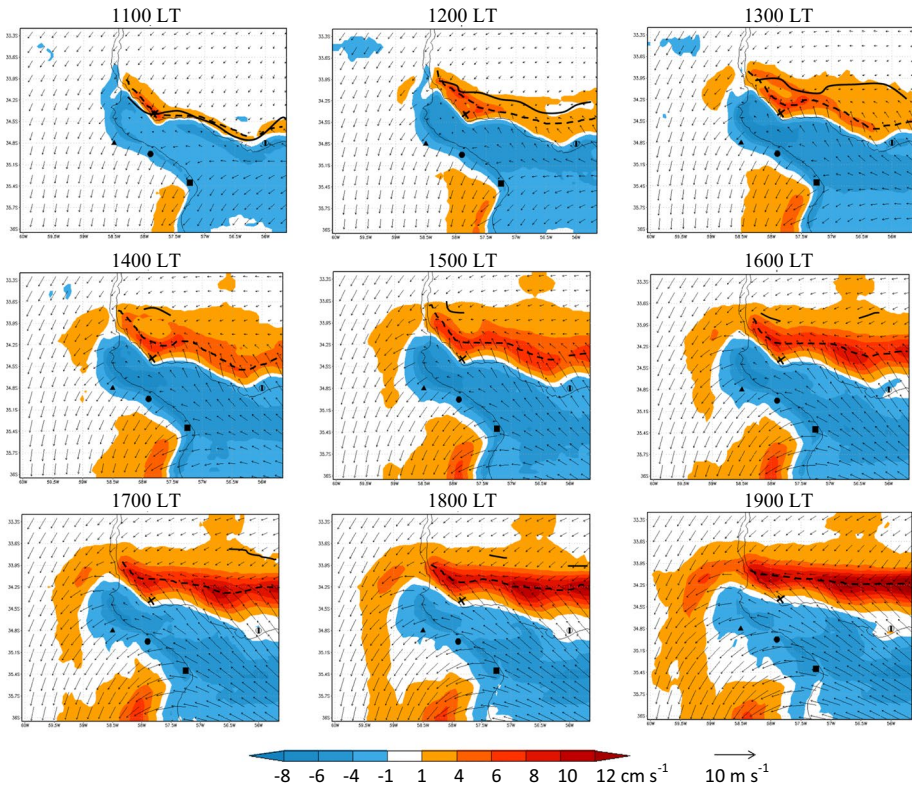
Fig. 9 Same as Fig. 8, but for the 7 November 2015 case

motion continues to deepen, while the region dominated of subsiding motion extends further inland in both coasts.

Figure 9 presents an analysis similar to that of Fig. 8, but for the 7 November 2015 case in the northern coast. Initially, regions of surface wind convergence and maximum upward motion develop inland the northern coast, while surface flow divergence and subsiding motion dominate over the river. At the beginning, both the SBrF and the WmxF are located near the northern coast and move inland, but the SBrF does it faster, as in the 11 January 2016 case. Until the early afternoon the SBrF is clearly defined, but after 1400 LT it disappears, while a well-defined WmxF continues to strengthen, but becomes almost stationary in the afternoon. In order to determine more precisely the SBrF inland progression, Fig. 10 outlines the SBrF distance to the coast versus time, along the transects of Fig. 7a.

The average speed at which the SBrF moves inland is calculated as the ratio of the maximum inland excursion of the front to the elapsed time of Fig. 10, and the results are presented in Table 4. On the southern coast (Fig. 10a), the average SBrF speed along the PIN transect (closest to the river mouth) is 6.0 m s^{-1}, twice the speed along the other two transects.

However, it should be noted that the SBrF position along the PIN transect is calculated up to 1400 LT, after which it begins to disappear, while along the other two transects it can be tracked for a few more hours. Initially, the SBrF appears to move at approximately the

(a) 11 January 2016 southern coast **(b)** 7 November 2015 northern coast
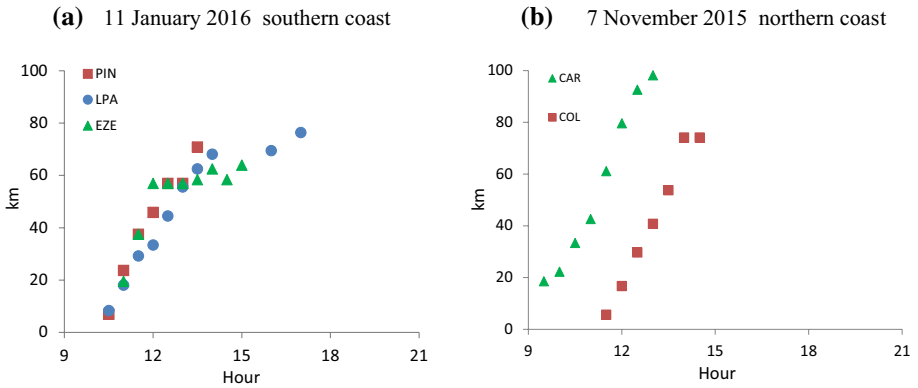
Fig. 10 SBrF distance to the coast versus time, along transects across weather stations: **a** EZE (green), LPA (blue) and PIN (red) for the 11 January 2016 case in the southern coast; and **b** CAR (green) and COL (red) for the 7 November 2015 case in the northern coast

Table 4 Averaged inland propagation speed of SBrF, WmxF and CloF along transects of Fig. 7a

Average speed (m s^{-1})	11 January 2016 southern coast			7 November 2015 northern coast	
	PIN	LPA	EZE	CAR	COL
SBrF	6.0	3.0	2.8	7.0	6.5
WmxF	2.6	2.2	1.9	2.1	1.8
CloF	2.5	2.2	2.1	2.7	1.7

(a) 11 January 2016 southern coast

(b) 7 November 2015 northern coast
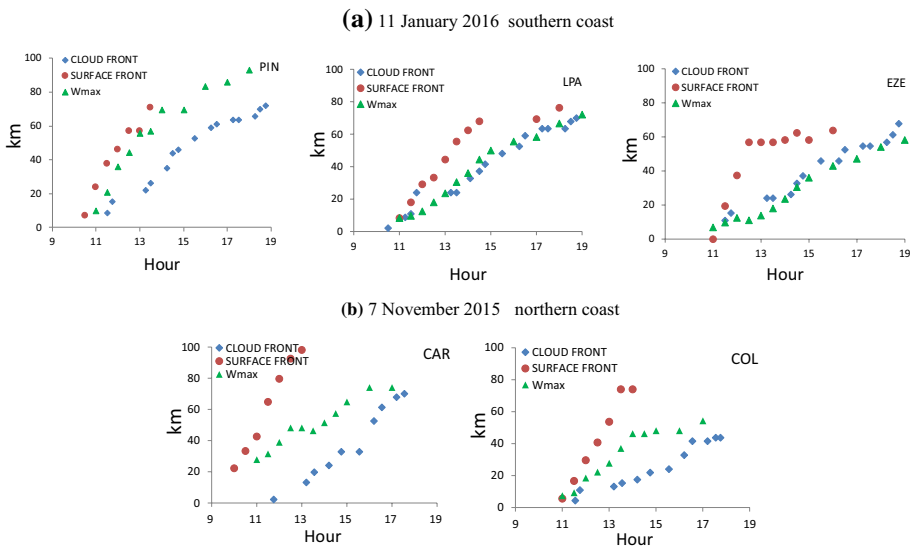
Fig. 11 Distance to the coast versus time of the SBrF, WmxF and CloF, along transects across **a** weather stations of the southern coast PIN, LPA and EZE for the 11 January 2016 case; and **b** weather stations of the northern coast CAR and COL for the 7 November 2015 case

same speed at all three locations, but later in the afternoon, it slows down along the LPA and EZE transects. In the northern coast (Fig. 10b), the SBrF inland speed is similar in both places: along the CAR transect (closer to the river mouth), it is 7.0 m s^{-1} and along COL transect (closer to the river source), it is 6.5 m s^{-1}. With the purpose of comparing with the speed of the different fronts, Fig. 11 presents plots of the SBrF, WmxF and CloF distance to the coast versus time, along the transects of Fig. 7a, and the resulting speeds are summarized in Table 4.

For the 11 January 2016 case in the southern coast (Fig. 11a), along the LPA transect the SBrF speed is 3.0 m s^{-1}, greater than that of CloF and WmxF (2.2 m s^{-1}). Along the EZE transect, despite a marked reduction after 1200 LT, the average SBrF speed is 2.8 m s^{-1}, also greater than that of CloF (2.1 m s^{-1}) and WmxF (1.9 m s^{-1}). In the case of PIN, the SBrF speed of 6.0 m s^{-1} is more than twice as high as that of the other two fronts. For the 7 November 2015 case on the northern coast (Fig. 11b), the SBrF speed along the CAR and COL transects is, as in the other case, much greater than that of WmxF (2.1 m s^{-1} at CAR, 1.8 m s^{-1} at COL), and that of CloF (2.7 m s^{-1} at CAR, 1.7 m s^{-1} at COL).

It is interesting to compare the SBrF speed obtained, with the results reported by other studies. Zhong and Takle (1992) estimate speeds of 2 m s^{-1} on the Florida peninsula that increase to 6 m s^{-1} in some areas in the mid-afternoon. Alpert and Rabinovich-Hadar (2003) found propagation speeds between 1.5 and 3 m s^{-1} near the Mediterranean coast of Israel that increase to 10 m s^{-1} about 20 km inland. Bastin and Drobinski (2006) find speeds of 2.7 m s^{-1} at the south coast of France, and Freitas et al. (2007) in the coastal region of Sao Paulo, Brazil, calculate a sea-breeze front speed of 2.5 m s^{-1}. Azorin-Molina and Chen (2009), in a study on the Mediterranean coast of Spain for several years, determine a maximum inland penetration of 120 km with an average duration of 12 h, which provides a maximum average speed of 2.8 m s^{-1}. In the present study, the calculated sea-breeze speeds at the surface range from 2.8 to 6.1 m s^{-1} and are within the range of values reported by other studies.

The SBrF moves inland faster towards the river mouth than the river source, in particular on the southern coast the difference is more marked. The intensity of the sea breeze should be greater in areas closer to the Atlantic Ocean that are subject to a greater sea–land thermal contrast since the temperature of the ocean waters is always a few degrees lower than the river waters (Guerrero et al. 2010). However, the SBrF speed at COL, in the northern coast, is much greater than that at EZE and LPA on the southern coast (see Fig. 2a), despite being at about the same distance from the open ocean. The three places where the SBrF moves forward faster (i.e., COL, CAR and PIN), are in regions with a coastal convexity towards the river and the ocean that enhances the low-level convergence. This coastline feature would explain the difference between SBrF speeds along the transects of both coasts near the river source.

Figure 12 shows the inland progression during the afternoon of the WmxF (dotted line) and CloF (dashed line) on both coasts. Regardless the presence of some high level clouds, particularly during the afternoon of 7 November 2015, it is possible to outline quite precisely the CloF position as a continuous line over the region. Figure 13 outlines the SBrF and WmxF inland progression between 1100 and 1400 LT when the SBrF is better defined, and on both coasts the SBrF moves forward faster than the WmxF. Also, both fronts propagate further inland towards the Atlantic Ocean than the river source, probably due, as discussed, to the greater thermal contrast there. In both cases, boundary layer clouds (small cells) can be seen from mid-morning almost everywhere over land but not over the river. These clouds are formed by the shallow convection that develops over land because of the

(a) 11 January 2016 southern coast

(b) 7 November 2015 northern coast
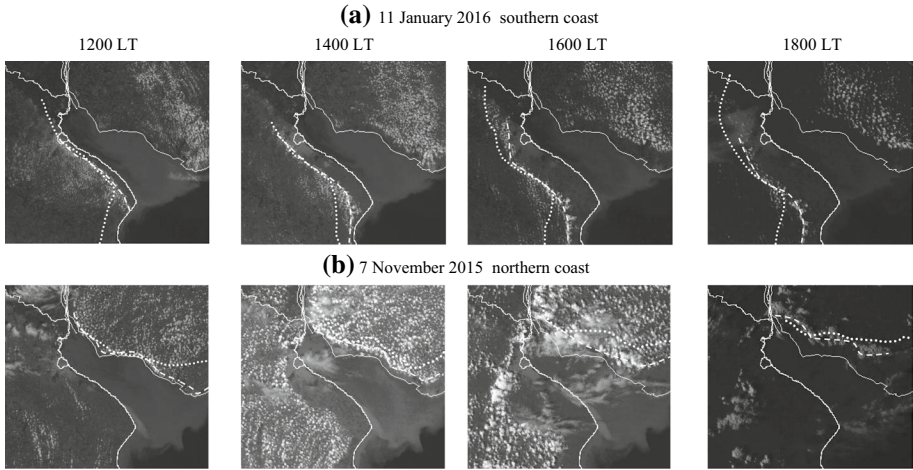
Fig. 12 Sequence of GOES-13 images outlining the WmxF (dotted line) and CloF (dashed line) for **a** the 11 January 2016 case in the southern coast; and **b** the 7 November 2015 case in the northern coast

SBrF inland progression   WmxF inland progression

(a) 11 January 2016   southern coast

(b) 7 November 2015   northern coast
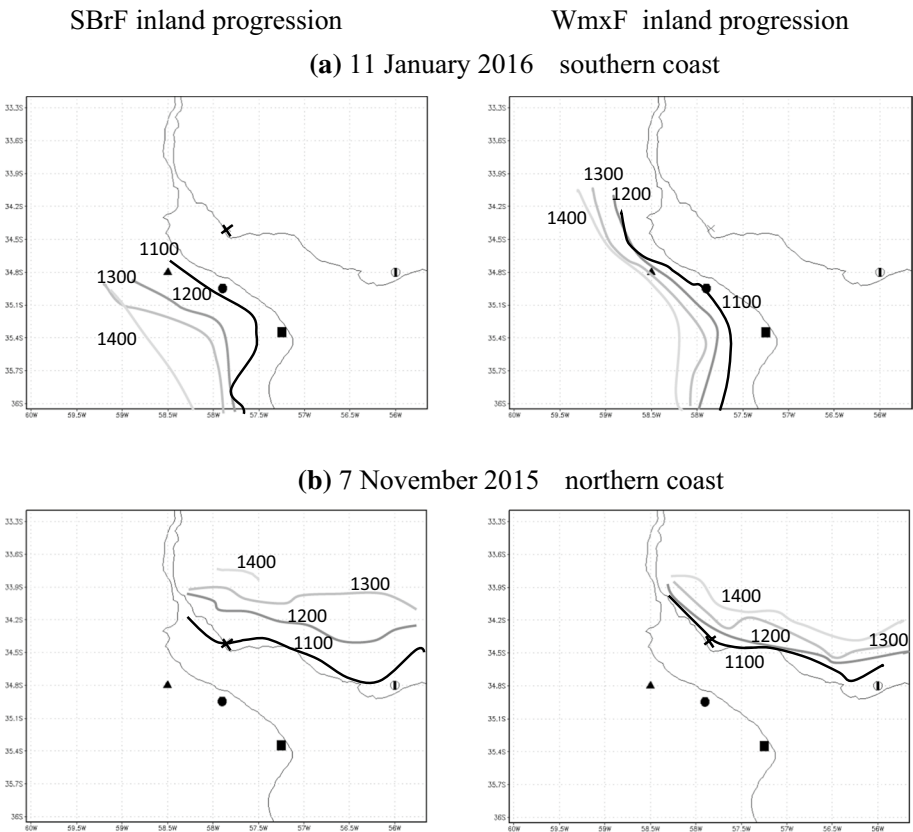
Fig. 13 Inland progression with time of the SBrF (left panels) and WmxF (right panels) for **a** the 11 January 2016 on the southern coast; and **b** the 7 November 2015 on the northern coast

surface heating due to mostly clear skies since early morning, but not because of the sea-breeze circulation itself that by mid-morning is still confined near the coasts.

As discussed in Sect. 4, the sea breeze is a wedge of cooler and denser sea air that moves inland, creating a sea-breeze front that tilts with height towards the sea (Simpson 1994). The subsidence region that develops a few 100 m above the surface sea-breeze front and behind is what inhibits the cloud formation. The boundary-layer clouds seen in the satellite imagery were already present everywhere over land before the arrival of the sea-breeze front, so that the continuously growing cloudless region behind it, whose edge defines the CloF, simply follows the inland progression of the sea breeze.

The inland propagation speeds of WmxF and CloF are very similar at the five locations (see Table 4), which indicates that associating the inland progression of the region of maximum upward motion with the cloud pattern changes of the satellite imagery is appropriate. On the other hand, the CloF and WmxF propagation speeds are always smaller than that of the SBrF. This may be in part due to the complex structure of the sea-breeze front that, as discussed by Simpson (1994), develops gravity waves in the interphase between the cooler and denser sea air below and the warmer and less dense land air above. But, the difference between the speeds of the surface sea-breeze front and the other fronts aloft may also be a consequence of the method used to calculate the SBrF position along the transects, whose changes with time define the propagation speed. As noted at the beginning of this section, the SBrF position is determined by the point that shows a wind direction change of at least 30° from the previous hour. Certainly, choosing a different magnitude of wind direction change could result in a different propagation speed.

6 Summary and Conclusions

Two well-developed sea-breeze cases from the La Plata River region are studied using local observations, satellite imagery and hydrostatic boundary layer model simulations. The sea-breeze cases are selected from a recent 5-month summer period with the following criteria. First, MODIS images from the afternoon are used to identify days with boundary layer cloud bands typically associated with sea-breeze circulations. Then, the analysis of local observations and regional meteorological conditions allowed filtering the appropriate days, following the criteria often used in other sea-breeze studies.

The two selected cases, from both the northern and southern coast, are characterized by offshore regional winds that help develop stronger sea breezes due to enhanced horizontal convergence by the opposing winds. The two cases are simulated with the model forced by operational Eta regional forecasts, and the wind and temperature forecasts are validated with local observations. The selection procedure based on the analysis of cloud patterns of satellite images, targets the specific cases for which the dry model is likely to be relevant and perform well.

The model surface wind fields are used to define the SBrF, the vertical velocity fields at 1000 m are used to delimit the region of maximum upward motion that defines the WmxF, and GOES-13 images are used to outline the CloF. The time sequences of the model outputs and GOES-13 images allow the SBrF, WmxF, and CloF positions to be determined along five transects and to calculate their inland propagation speed. On the southern coast, the SBrF moves inland at twice the speed towards the river mouth (6.0 m s^{-1}) than the river source (2.8 m s^{-1}), probably due to the higher thermal contrast with the Atlantic Ocean waters. This difference is not evident in the northern coast, since there are only two

meteorological stations, and the one closer to the river source is located in an area with a coastal convexity towards the river that makes it a preferential region of convergence that enhances the sea-breeze strength.

The SBrF moves inland with a variable speed between 2.8 and 7.0 m s^{-1}, in general in agreement with other studies, but more than twice as fast as that of the other two fronts. The difference may be due, in addition to the complex nature of the phenomenon, to the method used to determine the SBrF position along the transects, whose changes with time define the propagation speed. The point along the transects showing a wind direction change of at least 30° from the previous hour determines the SBrF position, so choosing a different magnitude of wind direction change could result in a different propagation speed.

In both cases, boundary-layer clouds are present from mid-morning almost everywhere on land but not over the river, and they develop due to the strong surface heating with mostly clear skies. The cooler, denser marine air moves inland as the sea-breeze front advances, creating a subsidence region behind that inhibits cloud formation. The boundary layer clouds seen in satellite imagery since mid-morning were already present before the arrival of the sea-breeze front, so that the continuously growing cloudless region behind it, whose edge defines the CloF, simply follows the inland progression of the sea breeze.

The inland propagation speeds of WmxF and CloF are very similar to each other and less variable throughout the region, indicating that the modelled progression of the maximum vertical motion in both cases reproduces the inland propagation speed of the cloud bands evident in satellite imagery relatively well. The study shows that the sea-breeze propagation accompanies changes in the three-dimensional circulation of the boundary layer, and that relating the model-derived vertical motion field with the cloud front of the satellite imagery is valid. The overall conclusion of the study is that simulations with a dry hydrostatic boundary-layer model can be useful to analyze the regional scale characteristics of three-dimensional sea-breeze circulation and its changes over time in regions with simple topography.

References

Alpert P, Rabinovich-Hadar M (2003) Pre-and post-sea-breeze frontal lines—a Meso-γ-scale analysis over South Israel. J Atmos Sci 60:2994–3008

Arritt RW (1993) Effects of the large-scale flow on characteristic features of the sea breeze. J Appl Meteorol 32:116–125

Atkinson BW (1981) Meso-scale atmospheric circulations. Academic Press, London

Azorin-Molina C, Chen D (2009) A climatological study of the influence of synoptic-scale flows on sea breeze evolution in the Bay of Alicante (Spain). Theor Appl Climatol 96:249–260

Banta RM, Lisa DO, Levinson DH (1993) Evolution of the Monterey Bay sea-breeze layer as observed by pulsed Doppler lidar. J Atmos Sci 50:3959–3982

Barbato JP (1978) Areal parameters of the sea breeze and its vertical structure in the Boston basin. Bull Am Meteorol Soc 59:1420–1431

Bastin S, Drobinski P (2006) Sea-breeze-induced mass transport over complex terrain in south-eastern France: a case-study. Q J R Meteorol Soc 132:405–423

Bastin S, Drobinski P, Dabas A, Delville P, Reitebuch O, Werner C (2005) Impact of the Rhône and Durance valleys on sea-breeze circulation in the Marseille area. Atmos Res 74:303–328

Berri GJ, Bertossa G (2018) Initializing a mesoscale boundary-layer model with radiosonde observations. Boundary-Layer Meteorol 166:137–151

Berri GJ, Nuñez MN (1993) Transformed shoreline following horizontal coordinates in a mesoscale model: a sea land breeze case study. J Appl Meteorol 32:918–928

Berri GJ, Sraibman L, Tanco R, Bertossa G (2010) Low-level wind field climatology over the La Plata River region obtained with a mesoscale atmospheric boundary layer model forced with local weather observations. J App Meteorol Climatol 49:1293–1305

Berri GJ, Galli Nuin J, Sraibman L, Bertossa G (2012) Verification of a synthesized method for the calculation of low-level climatological wind fields using a mesoscale boundary-layer model. Boundary-Layer Meteorol 142:329–337

Borne K, Chen D, Nunez M (1998) A method for finding sea breeze days under stable synoptic conditions and its application to the Swedish west coast. Int J Climatol 18:901–914

Chen F, Miao S, Tewari M, Bao JW, Kusaka H (2011) A numerical study of interactions between surface forcing and sea breeze circulations and their effects on stagnation in the greater Houston area. J Geophys Res 116(D12105). https://doi.org/10.1029/2010JD015533

Chen G, Iwai H, Ishii S, Saito K, Seko H, Sha W, Iwasaki T (2019) Structures of the sea-breeze front in dual-Doppler lidar observation and coupled mesoscale-to-LES modeling. J Geophys Res Atmos 124:2397–2413

Comer NT, McKendry IG (1993) Observations and numerical modeling of Lake Ontario lake breezes. Atmos-Ocean 31:481–499

Cressman GP (1959) An operational objective analysis system. Mon Weather Rev 87:367–878

Crosman ET, Horel JD (2010) Sea and lake breezes: a review of numerical studies. Boundary-Layer Meteorol 137:1–29

Defant F (1951) Compendium of meteorology. American Meteorological Society, Providence, pp 658–672

Estoque MA (1962) The sea breeze as a function of the prevailing synoptic situation. J Atmos Sci 19:244–250

Federico S, Pasqualoni L, De Leo L, Bellecci C (2010) A study of the breeze circulation during summer and fall 2008 in Calabria, Italy. Atmos Res 97:1–13

Finkele K (1998) Inland and offshore propagation speeds of a sea breeze from simulations and measurements. Boundary-Layer Meteorol 87:307–329

Finkele K, Hacker JM, Kraus H, Byron-Scott RA (1995) A complete sea-breeze circulation cell derived from aircraft observations. Boundary-Layer Meteorol 73:299–317

Freitas ED, Rozoff CM, Cotton WR, Silva Dias PL (2007) Interactions of an urban heat island and sea-breeze circulations during winter over the metropolitan area of São Paulo, Brazil. Boundary-Layer Meteorol 122:43–65

Frizolla JA, Fisher EL (1963) A series of sea breeze observations in the New York City area. J Appl Meteorol 2:722–739

Furberg M, Steyn DG, Baldi M (2002) The climatology of sea breezes on Sardinia. Q J R Meteorol Soc 22:917–932

Guerrero RA, Piola AR, Molinari GN, Osiroff AP, Jauregui SI (2010) Climatologia de temperatura y salinidad en el Rio de La Plata y su frente maritimo. Argentina-Uruguay. Mar del Plata: Instituto Nacional de Investigacion y Desarrollo Pesquero INIDEP, Argentina, 95 pp

Harris L, Kotamarthi VR (2005) The characteristics of the Chicago Lake breeze and its effects on trace particle transport: results from an episodic event simulation. J Appl Meteorol 44:1637–1654

Kanamitsu M, Ebisuzaki W, Woollen J, Yang S-K, Hnilo JJ, Fiorino M, Potter GL (2002) NCEP-DOE AMIP-II Reanalysis (R-2). Bull Am Meteorol Soc 83:1631–1644

Keen CS, Lyons QA (1978) Lake/land breeze circulations on the western shore of Lake Michigan. J Appl Meteorol 17:1843–1855

Kunhikrishnan PK, Ramachandran R, Alappattu DP, Kumar NK, Balasubrahamanyam D (2006) A case study of sea breeze circulation at Thumba Coast through observations and modelling. Remote sensing and modeling of the atmosphere, oceans, and interactions. Int Soc Opt Photonics 6404:640417

Lyons WA (1972) The climatology and prediction of the Chicago lake breeze. J Appl Meteorol 11:1259–1270

Lyons WA, Tremback CJ, Pielke RA (1995) Applications of the Regional Atmospheric Modeling System (RAMS) to provide input to photochemical grid models for the Lake Michigan Ozone Study (LMOS). J Appl Meteorol 34:1762–1786

Martin CL, Pielke RA (1983) The adequacy of the hydrostatic assumption in sea breeze modeling over flat terrain. J Atmos Sci 40:1472–1481

Miao JF, Kroon LJM, de Arellano JVG, Holtslag AAM (2003) Impacts of topography and land degradation on the sea breeze over eastern Spain. Meteorol Atmos Phys 84:157–170

Miller STK, Keim BD, Talbot RW, Mao H (2003) Sea breeze: structure, forecasting, and impacts. Rev Geophys. https://doi.org/10.1029/2003RG000124

Nicholls ME, Pielke RA, Cotton WR (1991) A two-dimensional numerical investigation of the interaction between sea breezes and deep convection over the Florida peninsula. Mon Weather Rev 119:298–323

Orlanski I (1981) The quasi-hydrostatic approximation. J Atmos Sci 38:572–582

Papanastasiou DK, Melas D, Lissaridis I (2010) Study of wind field under sea breeze conditions; an application of WRF model. Atmos Res 98:102–117

Phan TT, Manomaiphiboon K (2012) Observed and simulated sea breeze characteristics over Rayong coastal area, Thailand. Meteorol Atmos Phys 116:95–111

Pielke R (2002) Mesoscale meteorological modelling. Academic Press, London, 676 pp

Planchon O, Damato F, Dubreuil V, Gouéry P (2006) A method of identifying and locating sea-breeze fronts in north-eastern Brazil by remote sensing. Meteorol Appl 13:225–234

Prtenjak MT, Grisogono B (2007) Sea-land breeze climatological characteristics along the northern Croatian Adriatic coast. Theor Appl Climatol 90:201–215

Ratto G, Berri GJ, Maronna R (2014) On the application of hierarchical cluster analysis for synthesizing low-level wind fields obtained with a mesoscale boundary layer model. Meteorol Appl 21:708–716

Shafran PC, Seaman NL, Gayno GA (2000) Evaluation of numerical predictions of boundary layer structure during the Lake Michigan Ozone Study. J Appl Meteorol 39:412–426

Simpson JE (1994) Sea breeze and local winds. Cambridge University Press, Cambridge, 234 pp

Sraibman L, Berri GJ (2009) Low level wind forecast over La Plata River region with a mesoscale boundary layer model forced by regional operational forecasts. Boundary-Layer Meteorol 130:407–422

Srinivas CV, Venkatesan R, Somayaji KM, Singh AB (2006) A numerical study of sea breeze circulation observed at a tropical site Kalpakkam on the east coast of India, under different synoptic flow situations. J Earth Syst Sci 115:557–574

Wakimoto RM, Atkins NT (1994) Observations of the sea-breeze front during CAPE. Part I: single-Doppler, satellite, and cloud photogrammetry analysis. Mon Weather Rev 122:1092–1114

Wilks DS (2011) Statistical methods in the atmospheric sciences. Academic Press, London, 704 pp

Xun-lai C, Ye-rong F, Jiang-nan L, Wen-shi L, Shao-jia F, An-yu W, Hui L (2009) Numerical simulations on the effect of sea–land breezes on atmospheric haze over the Pearl River Delta Region. Environ Model Assess 14:351–363

Zhong S, Takle ES (1992) An observational study of sea-and land-breeze circulation in an area of complex coastal heating. J Appl Meteorol 31:1426–1438